Nano Research 2017, 10(8): 2743–2760
DOI 10.1007/s12274-017-1478-6
Research Article
ISSN 1998-0124
CN 11-5974/O4

Biocompatible custom ceria nanoparticles against reactive oxygen species resolve acute inflammatory reaction after intracerebral hemorrhage

Dong-Wan Kang[1,2,§], Chi Kyung Kim[1,3,§], Han-Gil Jeong[1,2,§], Min Soh[4,5], Taeho Kim[4,5], In-Young Choi[1,2], Seul-Ki Ki[1,2], Do Yeon Kim[1,2], Wookjin Yang[1,2], Taeghwan Hyeon[4,5], and Seung-Hoon Lee[1,2] (✉)

[1] *Laboratory of Innovative Nanobiotechnology, Biomedical Research Institute, Seoul National University Hospital, Seoul 03080, Republic of Korea*
[2] *Department of Neurology, Seoul National University Hospital, Seoul 03080, Republic of Korea*
[3] *Department of Neurology, Korea University Guro Hospital and Korea University College of Medicine, Seoul 08308, Republic of Korea*
[4] *Center for Nanoparticle Research, Institute for Basic Science (IBS), Seoul 151-742, Republic of Korea*
[5] *School of Chemical and Biological Engineering and Institute of Chemical Processes, Seoul National University, Seoul 151-742, Republic of Korea*
[§] *These authors contributed equally to this work.*

Received: 28 June 2016
Revised: 4 January 2017
Accepted: 9 January 2017

KEYWORDS
ceria nanoparticles, intracerebral hemorrhage, free radical injury, anti-inflammation, neuroprotective agents, biomedical application

ABSTRACT

Intracerebral hemorrhage (ICH) is a devastating subtype of stroke with a high mortality rate, for which there currently is no effective treatment. A perihematomal edema caused by an intense inflammatory reaction is more deleterious than the hematoma itself and can result in neurological deterioration and death. Ceria nanoparticles (CeNPs) are potent free radical scavengers with potential for biomedical applications. As oxidative stress plays a major role in post-ICH inflammation, we hypothesized that CeNPs might protect against ICH. To test this hypothesis, core CeNPs were synthesized using a modified reverse micelle method and covered with phospholipid-polyethylene glycol (PEG) to achieve biocompatibility. We investigated whether our custom-made biocompatible CeNPs have protective effects against ICH. The CeNPs reduced oxidative stress, hemin-induced cytotoxicity, and inflammation *in vitro*. In a rodent ICH model, intravenously administered CeNPs were mainly distributed in the hemorrhagic hemisphere, suggesting that they could diffuse through the damaged blood–brain barrier. Moreover, CeNPs attenuated microglia/macrophage recruitment around the hemorrhagic lesion and inflammatory protein expression. Finally, CeNP treatment reduced the brain edema by 68.4% as compared to the control. These results reveal the great potential of CeNPs as a novel therapeutic agent for patients with ICH.

Address correspondence to sb0516@snu.ac.kr

1 Introduction

Intracerebral hemorrhage (ICH) is the second most common subtype of stroke, comprising approximately 20% of all stroke cases, and 10–30 new cases per 100,000 individuals are reported annually [1, 2]. Despite the high mortality rate of 30% in ICH patients [3], few treatment modalities are currently available, except for simply lowering blood pressure [4]. Several treatment strategies to reduce hematoma size have been attempted, but all were unsuccessful. Surgical removal of a hematoma was not effective because of its deep-seated location and potential complications of surgery [5]. Moreover, recombinant activated factor VII, a hemostatic agent for halting hematoma growth, did not improve survival or functional outcome in a phase 3 trial [6]. Thus, inflammation in the perihematomal area, not the hematoma itself, has emerged as a new therapeutic target, since secondary brain injury due to inflammation is as important as the primary mass effect of the hematoma [7]. Release of clot components such as hemoglobin and thrombin after the initial hemorrhage trigger secondary cascades leading to deterioration owing to oxidative stress, inflammation, and edema formation [8, 9]. Although most patients survive in the initial phase of hemorrhage, secondary brain injury caused by the inflammation and perihematomal edema result in severe neurological deficits or death [10]. Thus, many researchers have attempted to identify therapies that can reduce or prevent secondary brain injury due to inflammation in ICH.

Cerium is a rare earth element in the lanthanide series that is used in catalytic converters for automobile exhaust systems and other commercial applications because of its strong redox capacity [11]. Ceria nanoparticles (CeNPs) with a large surface-to-volume ratio have been highlighted as novel therapeutic agents for diseases related to oxidative damage, including retinal degeneration, spinal cord injury, and endothelial injury [12–14]. These nanoparticles can be modified to be biocompatible using specific formulation techniques and surface modulation [15]. Furthermore, CeNPs have been reported to have general anti-inflammatory effects in addition to their anti-oxidative effects, which may expand their range of applications to include various diseases related to inflammation [16–20].

Previously, we synthesized small, uniform, and highly biocompatible custom-made phospholipid-polyethylene glycol (PEG)-capped CeNPs with potent anti-oxidant effects, which showed strong and robust therapeutic effects in animal models of ischemic stroke via reducing oxidative brain injury [21]. Reactive oxygen species (ROS) also play a key role in the inflammation development in ICH [22]. Thus, we investigated the therapeutic effects of these nanoparticles in ICH, focusing on the ICH-specific anti-inflammatory function of the CeNPs through their ROS scavenging effect.

2 Experimental

2.1 Reagents

Cerium (III) acetate hydrate, xylene (98.5%), and rhodamine B isothiocyanate (RITC) were purchased from Sigma-Aldrich Inc. (St. Louis, MO, USA). Oleylamine (approximate C18-content of 80%–90%) was purchased from Acros Organics (Geel, Belgium). Chloroform (99%) and acetone (99%) were purchased from Samchun Chemicals (Gyeonggi-do, South Korea). 1,2-Distearoyl-sn-glycero-3-phosphoethanol-amine-N-[methoxy(polyethylene glycol)-2000] (mPEG-2000 PE) and 1,2-distearoyl-sn-glycero-3- phosphoethanolamine-N-[amino(polyethylene glycol) -2000] (DSPE-PEG(2000) amine) were purchased from Avanti Polar Lipids Inc. (Alabaster, AL, USA).

2.2 Synthesis of CeNPs

Core CeNPs, phospholipid-PEG-capped CeNPs, and RITC-conjugated CeNPs (RITC-CeNPs) were synthesized as previously described [21]. Cerium (III) acetate hydrate (1 mmol, 0.4 g) and 12 mmol (3.2 g) oleylamine were added to 15 mL of xylene (98.5%). The mixture was sonicated for 15 min at room temperature and then heated to 90 ℃ at a heating rate of 2 ℃/min. To initiate the hydrolytic sol-gel reaction, 1 mL of deionized water was injected into the solution with vigorous stirring, at 90 ℃. The solution color changed from off-white to cloudy yellow over time, indicating that the reaction had proceeded. The reaction colloid was aged at 90 ℃ for 3 h, and then

cooled to room temperature. To remove organic residues, a washing step was required; acetone (100 mL) was added to wash and precipitate the CeNPs using centrifugation. The purified core CeNPs were stored in chloroform, at a final concentration of 10 mg/mL.

2.3 Synthesis of phospholipid-PEG-capped CeNPs

The core CeNPs dispersed in chloroform were made biocompatible by phospholipid-PEG encapsulation. First, 5 mL of core CeNPs in $CHCl_3$ (10 mg/mL) was mixed with 10 mL of mPEG-2000 PE in $CHCl_3$ (10 mg/mL). Then, the $CHCl_3$ was evaporated in a rotary evaporator followed by incubation at 70 ℃ in a vacuum oven for chloroform removal. 5 mL of water was added, resulting in a transparent colloidal suspension. After filtration through a 0.4-μm filter, excess mPEG-2000 PE was removed using ultracentrifugation. The purified phospholipid-PEG-capped CeNPs were dispersed in distilled water.

For conjugation of RITC, the core CeNPs must be encapsulated not only in a PEG-phospholipid shell, but also in an amine-functionalized PEG-phospholipid shell. Core CeNPs (5 mL) in $CHCl_3$ (10 mg/mL) were mixed with 9 mL of mPEG-2000 PE in $CHCl_3$ (10 mg/mL) and 1 mL of DSPE-PEG(2000) amine in $CHCl_3$ (10 mg/mL). The purification procedures used for phospholipid PEG encapsulation were applied to produce well-washed CeNPs dispersed in distilled water. After phospholipid-PEG conjugation, 5 mg of RITC was added to the colloidal suspension, and the mixed solution was stirred for 12 h at 40 ℃. After another round of filtration and ultracentrifugation, the RITC-CeNPs were dispersed in distilled water. As the CeNPs and RITC-CeNPs were synthesized in distilled water at a very high concentration (59.2 mM or 8.3 mg/mL), we diluted the solution with phosphate buffered saline (PBS) approximately 500 to 1,000 times for *in vitro* and 30 times for *in vivo* experiments.

2.4 Synthesis of phospholipid-PEG micelle vehicles

To form phospholipid-PEG vehicles, 20 mg mPEG-2000 PE in 4 mL of distilled water was vigorously stirred for 6 h. After filtration through a 0.4-μm filter, phospholipid-PEG vehicles (5 mg/mL) were made according to the critical micelle concentrations (CMC) of DSPE-PEG(2000). To form RITC-conjugated phospholipid-PEG vehicles, 18 mg mPEG-2000 PE and 2 mg DSPE-PEG(2000) amine in 4 mL of distilled water were vigorously stirred for 6 h. After filtration through a 0.4-μm filter, amine-functionalized phospholipid-PEG vehicles (5 mg/mL) were made. To attach RITC to the vehicles, 2 mg of RITC was added to the colloidal suspension, and the mixture was stirred for 12 h at 40 ℃. After another filtration, the RITC-conjugated phospholipid-PEG vehicles were finally generated.

2.5 Characterization of the nanoparticles

Transmission electron microscopy (TEM) at 200 kV (JEM-2100f; JEOL, Akishima, Japan) was used to determine the shapes and sizes of the core CeNPs. X-ray diffraction (XRD) patterns of core CeNPs were investigated using a D/Max-3C diffractometer (Rigaku, The Woodlands, TX, USA). Phase identification was performed using JCPDS-ICDD 2000 software. X-ray photoelectron spectroscopy (XPS) was carried out using an AXIS-HSi system (Kratos, Manchester, UK), and peaks were fitted using CasaXPS software. Dynamic light scattering (DLS) with a Zetasizer Nano-ZS system (Malvern Instruments, Inc., Malvern, UK) was used to measure the hydrodynamic diameters (HDs) and zeta potentials of the CeNPs and vehicles. The specific surface area (m^2/g) was measured using the Brunauer, Emmett, and Teller (BET) method with a TriStar™ II 3020 surface area analyzer (Micromeritics Instrument Corporation, Norcross, GA, USA).

2.6 Cell culture

Murine macrophage cell line RAW264.7 cells (ATCC® TIB-71™) were purchased from the American Type Culture Collection (Manassas, VA, USA), and cultured in Dulbecco's modified Eagle's medium (DMEM; Welgene, Daegu, Republic of Korea) containing 10% fetal bovine serum (FBS). U937 cells, a human leukemic monocyte lymphoma line, were purchased from the Korean cell line bank (Seoul, Republic of Korea), and cultured in Roswell Park Memorial Institute medium containing 10% FBS. Both cell lines were validated with a certificate at purchase and had been regularly tested for consistent cellular morphology and mycoplasma infection.

2.7 Superoxide anion assay

In vitro superoxide anion scavenging activity was assessed with a Superoxide Anion Assay kit (Sigma-Aldrich Inc., St. Louis, MO, USA). U937 cells were cultured for 48 h and activated by lipopolysaccharide (LPS) for 24 h, and a cell suspension was divided into each well of a 96-well plate (5.0×10^5 cells/well). The reaction was started by adding the reaction components (phorbol-12-myristate-13-acetate (PMA), enhancer solution, luminol solution, and buffer). CeNPs were added at the time of assay (0.05 and 0.1 mM; $n = 4$). We measured the superoxide anion-induced luminescence intensity every 5 min for 4 h. Four biologically independent experiments were conducted per group.

2.8 Dichlorodihydrofluorescein diacetate (DCF-DA) assay

We used DCF-DA (Molecular Probes, Eugene, OR, USA) fluorescence to measure the level of intracellular ROS. CeNPs (0.05 and 0.1 mM) were incubated with U937 cells 6 h before DCF-DA assay and H_2O_2 challenge. After incubation, the U937 cells were washed with PBS, suspended in 1 mL of prewarmed PBS (37 ℃) with 2 μM DCF-DA, and incubated for 20 min at 37 ℃. Then, H_2O_2 or PBS was added, and the cells were incubated for another 15 min at room temperature in the dark. We measured the intensity of DCF fluorescence by flow cytometry using a 488-nm laser for excitation, with detection at 535 nm. Four biologically independent experiments were carried out per group.

2.9 Nitric oxide (NO) assay

Nitrite (NO_2^-) release was assessed with a Griess reagent kit (Promega, Madison, WI, USA), which indicates the extent of NO production, as described previously [23]. In brief, RAW264.7 cells were prepared in 96-well plates at a density of 5×10^5 cells/well, and LPS with or without CeNPs (0.05 and 0.1 mM) was administered simultaneously. The assays were performed at 24 and 48 h. An equal volume of Griess reagent was added to the culture supernatant after treatment. Absorbance at 550 nm was read after 10 min of incubation at room temperature, and the NO_2^- concentration was interpolated from a standard curve generated with a series of concentrations of sodium nitrite ($NaNO_2$). We conducted four biologically independent experiments per group.

2.10 Western blot analysis

For the *in vitro* experiment, we stimulated RAW264.7 cells with 100 μM hemin with or without co-treatment with CeNPs (0.05 mM or 0.1 mM) for 24 h in DMEM with 1% FBS under incubation at 37 ℃ with 5% CO_2 in the dark. The cells were harvested by scraping and washed with cold PBS. For the *in vivo* experiment, in both the control and treatment groups, rats were sacrificed via decapitation and the brains were immediately collected. Cells or entire ipsilateral hemispheres were homogenized in radioimmunoprecipitation assay buffer. Then, 50 mg of protein was separated by 10% sodium dodecyl sulfate–polyacrylamide gel electrophoresis and transferred to nitrocellulose membranes. The membranes were incubated in blocking buffer (5% skim milk in 50 mmol/L Tris, pH 7.5, 0.15 mmol/L NaCl, and 0.05% Tween-20), and probed with antibodies recognizing cyclooxygenase-2 (COX-2) (ab15191; Abcam, Cambridge, UK) and α-actin (AP0060; Bioworld, Dublin, OH, USA). Peroxidase anti-rabbit IgG antibody (PI-1000; Vector Laboratories, Burlingame, CA, USA) was used as the secondary antibody. Immunoreactivity was visualized by enhanced chemiluminescence, and the relative optical densities were determined by comparison of the measured values for COX-2 and β-actin.

2.11 Lactate dehydrogenase (LDH) assay

We measured the level of cellular LDH release, and calculated the percentages of LDH release to measure the extent of cell membrane disruption, as described previously [24]. RAW264.7 cells were seeded in quadruplicate in 96-well plates at a density of 3×10^4 cells/well and were grown in culture medium for 24 h at 37 ℃. Thirty minutes before the assay, the culture medium was changed to phenol red-free DMEM containing 1% FBS to prevent albumin from binding to hemin. The total LDH content in the culture was determined after exposure to 2% Triton X-100. To each well, 100 μM of hemin was added to the culture media with co-treatment of CeNPs (0.05 or 0.1 mM) or PBS for 6 h, and the LDH assay was performed.

Four biologically independent experiments were conducted per group.

2.12 *In vitro* terminal deoxynucleotidyl transferase dUTP nick end labeling (TUNEL) assay

We used a TUNEL kit (Roche Applied Science, Penzberg, Germany) to detect apoptosis of RAW264.7 cells upon treatment with hemin. In brief, RAW264.7 cells were prepared in 8-well chamber slides at a density of 2×10^5 cells/chamber. In the positive control group, 100 μM of hemin was added, and 0.05 or 0.1 mM of CeNPs was additionally added in the treatment group. After 24 h, the cells were fixed with 4% paraformaldehyde and permeabilized with 0.1% Triton X-100 in 0.1% sodium citrate for 2 min at 2–8 °C. Then, 50 μL of TUNEL reaction mixture was added, and the cells were counter-stained with 4,6-diamidino-2-phenylindole (DAPI). We analyzed the samples by fluorescence microscopy (Leica DM5500B; Leica Biosystems Inc., Buffalo Grove, IL, USA). Four biologically independent experiments were carried out per group (four chambers per group), and we counted cells in five randomly selected fields at 200× magnification per chamber. In each field, approximately 300 to 500 cells were visualized. TUNEL-positive cells were counted by D. W. K. and C. K. K. who were blinded to group allocation.

2.13 Animals and experimental groups

We induced ICH in 8-week-old male Sprague-Dawley rats (200–250 g) as previously described [25]. In brief, under anesthesia with isoflurane, 0.5 units of collagenase VII (Sigma-Aldrich Inc., St. Louis, MO, USA) in 1 μL of saline was injected into the rats in the left striatum at the following stereotactic coordinates: 0.02 mm posterior and 0.30 mm lateral of the bregma, at 0.66 mm depth. The animals were randomly assigned to treatment groups after induction of ICH. CeNPs (0.5 mg/kg) or an equal volume of PBS was intravenously injected twice at 6 and 30 h after induction of ICH. Animals were excluded from the experimental group only if they died before sacrifice (in total, three animals were excluded from the study). The study was performed in the following stages. First, we sought to visualize the distribution of CeNPs using RITC-CeNPs and fluorescence microscopy. Second, to confirm the effect of the CeNPs on reduction of the inflammatory response, COX-2 expression was measured and CD68-positive microglia/macrophages were counted. Finally, hematoma volume and brain water content were measured to determine whether the CeNPs could reduce the final volume of the hematoma and the perihematomal edema. As previous studies have showed that perihematomal inflammation peaks at approximately 72 h after ICH [26], we examined the rodent ICH models at this time point in all experiments, except for the RITC-CeNP tracking experiments.

2.14 Tracking of CeNPs *in vivo*

After 6 h of ICH induction, 0.5 mg/kg of RITC- CeNPs or RITC-vehicle were administered to the rats via the tail vein. At 18 h after RITC-CeNP or RITC-vehicle injection (24 h after ICH induction, Fig. S1 in the Electronic Supplementary Material (ESM)), the rats were sacrificed and the brains were examined by immunofluorescence microscopy (Leica DM5500B; Leica Biosystems Inc.). Four independent experiments were performed in each group.

2.15 Visual augmentation using three-dimensional (3D) reconstruction

We conducted computerized visual augmentation using a 3D reconstruction of the fluorescence signals. After adding high-power field images (at 100× magnification) captured under 561-nm light, a raw image of a whole brain slice was created. Using MATLAB® (MATLAB® R2015b 8.6.0.267246, 64-bit, MathWorks, Inc., Natick, MA, USA), the 4,766 × 6,298 pixel truecolor image was converted to the grayscale intensity by forming a weighted sum of the R, G, and B components ($0.2989 \times R + 0.5870 \times G + 0.1140 \times B$). To construct a two-dimensional (2D) histogram, the image was gridded into 200 × 280-pixel squares, and the average grayscale intensity value of each grid was calculated considering the contours of the tissue slice. The relative fluorescence intensities were reported as the grayscale intensity versus the mean grayscale intensity of the image. Calculated (x, y) data values were computed to acquire kernel density estimates using a Gaussian low-pass size filter [1010] with a standard deviation of 100. 3D contour plots were

generated using the calculated (x, y, density) data values (Fig. S2 in the ESM).

2.16 Immunofluorescence staining and cell quantification

Seventy-two hours after ICH induction, the rats were anesthetized with isoflurane and transcardially perfused with PBS followed by 4% paraformaldehyde (PFA). After the brains were harvested and immersed in 4% PFA for 24 h, they were cryoprotected in 30% sucrose in PBS, and 40-μm coronal sections were prepared using a cryostat at –20 ℃. We selected a representative section from each animal. Assuming that the hematoma was spherical in shape, a coronal brain section immediately adjacent to the needle tract was selected, which likely included the center of hematoma. Each section was incubated with 0.5% bovine serum albumin/0.3% Triton-X. Non-specific antibody binding was blocked using 10% normal serum in PBS for 1 h. The sections were incubated with the primary antibody at 4 ℃ for 16 h. CD68 (ab125212; Abcam) was used as the primary antibody to label microglia/macrophages, and nuclei were visualized with DAPI. After washing, sections were incubated with Alexa Fluor® 488 goat anti-rabbit IgG (A11008, Invitrogen) secondary antibody for 2 h at room temperature. Seven biologically independent experiments were included for each group, and one representative section for each animal was investigated.

The perihematomal area was defined as the area where the morphology of the normal tissue and the integrity of cell density as visualized by DAPI were preserved (Fig. S3 in the ESM). The entire perihematomal area was analyzed by fluorescence microscopy (Leica DM5500B; Leica Biosystems Inc.) [27]. Semi-automated quantitative analysis of the CD68-positive cells was conducted using the ImageJ software (ImageJ 1.50c4; National Institutes of Health, Bethesda, MD, USA) by two independent investigators (D. W. K. and C. K. K) who were blinded to group allocation.

2.17 Measurement of hematoma volume

Seventy-two hours after ICH induction, the brains were cut coronally through the needle entry site (identifiable on the brain surface), and serial slices (1-mm thickness) both anterior and posterior to the needle entry site were obtained. Digital photographs of the serial slices were taken, and the hemorrhage volume was measured using ImageJ. The total hemorrhage volume (mm^3) was calculated by summing the clot area in each section and multiplying the sum by the distance between sections (Fig. S4 in the ESM) [28]. In addition, the volume of hemorrhage relative to the volume of contralateral hemisphere was measured. Four independent experiments were conducted per group.

2.18 Analysis of brain water content

Seventy-two hours after ICH induction, when brain injury is maximal [29], the brains were divided into the two hemispheres along the midline, and the cerebellum and brainstem were removed. The hemorrhagic hemispheres were immediately weighed on an electronic analytical balance to obtain the wet weight and then dried in a gravity oven at 100 ℃ for 24 h to obtain the dry weight. The water content of the hemorrhagic hemisphere was expressed as a percentage of the wet weight using the following formula: [(wet weight – dry weight) / (wet weight)×100]. Moreover, to adjust for individual brain size, the relative water content increase was calculated as the difference in brain water content between the ipsilateral and contralateral hemispheres of each animal. Five or six independent experiments were conducted per group.

2.19 Statistical analysis

All statistical analyses were performed using GraphPad Prism software (v6.01; GraphPad Software Inc., San Diego, CA, USA). Sample size was based on prior data and the results of a power calculation. All data are expressed as the mean ± standard error of the mean (s.e.m.). Statistical significance was analyzed using Student's t-test or one-way analysis of variance followed by the post-hoc Bonferroni's multiple comparisons test, as appropriate. Differences were considered significant at $P < 0.05$.

2.20 Study approval

All experimental procedures were approved by the Seoul National University Hospital Institutional

Animal Care and Use Committees (Approval number 15-0011-S1A0(2)).

3 Results

3.1 Development of phospholipid-PEG-capped CeNPs

We synthesized custom CeNPs as previously described [21]. The characteristics of our custom CeNPs are summarized in Table 1. TEM observation showed uniform 3-nm core CeNPs (Figs. S5(a)–S5(e) in the ESM).

High-resolution TEM showed that the nanoparticles produced a highly crystalline cross-lattice pattern. The XRD pattern showed that the core CeNPs possessed a cubic fluorite structure (Fig. S5(e) and Table S1 in the ESM). In the XPS analysis, the peaks of Ce^{3+} appeared at 885 and 903 eV, whereas those of Ce^{4+} appeared at 882, 898, 900, and 916 eV, and the surface Ce^{3+}/Ce^{4+} ratio was 0.43 (Fig. S6 in the ESM). To produce hydrophilic nanoparticles, the core CeNPs were PEGylated with mPEG-2000 PE. The phospholipid-PEG-capped CeNPs were 9.3 nm in HD with 35.4 mV in water, and 16.4 nm in PBS, were highly crystalline, and remained highly dispersed, with little agglomeration, in both physiological media and plasma for more than 10 days [21]. The HDs of the vehicles and the RITC-conjugated vehicles without core CeNPs were 1.3 and 11.8 nm, respectively, demonstrating the formation of micelles in water (Fig. S7 in the ESM)

3.2 Anti-oxidative effect of CeNPs *in vitro*

Schematic diagrams for *in vitro* experiments are provided in Fig. S8 (in the ESM). The anti-oxidative effect of the CeNPs was quantified using superoxide anion and DCF-DA assays. The DCF-DA assay was conducted to measure the total intracellular ROS (H_2O_2, hydroxyl radical $OH^{\cdot}$, and peroxynitrite $ONOO^{-}$) content [30]. We treated CeNPs to U937 cells for 6 h to investigate their effect on endogenous or exogenous ROS inside cells. CeNPs reduced the level of intracellular ROS in U937 cells as compared to the control (mean fluorescence intensity (MFI) of 76.6% ± 4.6% at 0.05 mM, 75.5% ± 0.6% at 0.1 mM, and 96.2% ± 2.4% in control; $P < 0.01$; Fig. 1(a)). When exogenous H_2O_2 was added, the CeNPs also reduced the level of intracellular ROS as compared to the control (MFI of 259.1% ± 6.1% at 0.05 mM, 287.9% ± 5.0% at 0.01 mM, and 380.3% ± 7.9% in the control; $P < 0.01$, Fig. 1(b)). In the superoxide anion assay, the CeNPs significantly reduced the generation of superoxide anions as compared to PBS after stimulation of LPS-primed U937 cells with PMA (Fig. 1(c)). No dose-response relationship was observed in both assays.

Table 1 Characteristics of custom CeNPs

Particle characteristics	CeNPs
Morphology	Round
Crystalline property	Cubic fluorite structure
Core size (TEM) (nm)	3–4
Hydrodynamic radii (nm)	9.3 ± 2.9 (water) 16.4 ± 3.2 (PBS)
Zeta-potential (mV)	35.4 ± 12.1
Surface Ce^{3+}/Ce^{4+} ratio	0.43
BET (m^2/g)	88.9

3.3 NO reduction of CeNPs *in vitro*

NO is an important inflammatory mediator [31]. We measured nitrite, which is an inert metabolite of NO, using Griess reagent. When the CeNPs were co-administered with 1 μg/mL of LPS to RAW264.7 cells, the amounts of nitrite at 24 and 48 h were markedly reduced as compared to the LPS-only-treated group (Fig. 1(d)). The nitrite-reducing effect was consistent at doses above 0.05 mM CeNPs, and no significant difference was observed between the low-dose (0.05 mM) and high-dose (0.1 mM) CeNP-treated groups.

3.4 Anti-inflammatory and cytoprotective effects of CeNPs in an *in vitro* ICH model

To investigate whether the CeNPs could reduce the hemin-induced inflammatory reaction [32], we measured the level of COX-2, the key enzyme responsible for the conversion of arachidonic acid to prostaglandin [33]. When co-administered with 100 μM hemin for 24 h in RAW264.7 cells, 0.1 mM of CeNPs significantly inhibited the expression of COX-2 protein as compared to that in the hemin-only group (65.5% ±

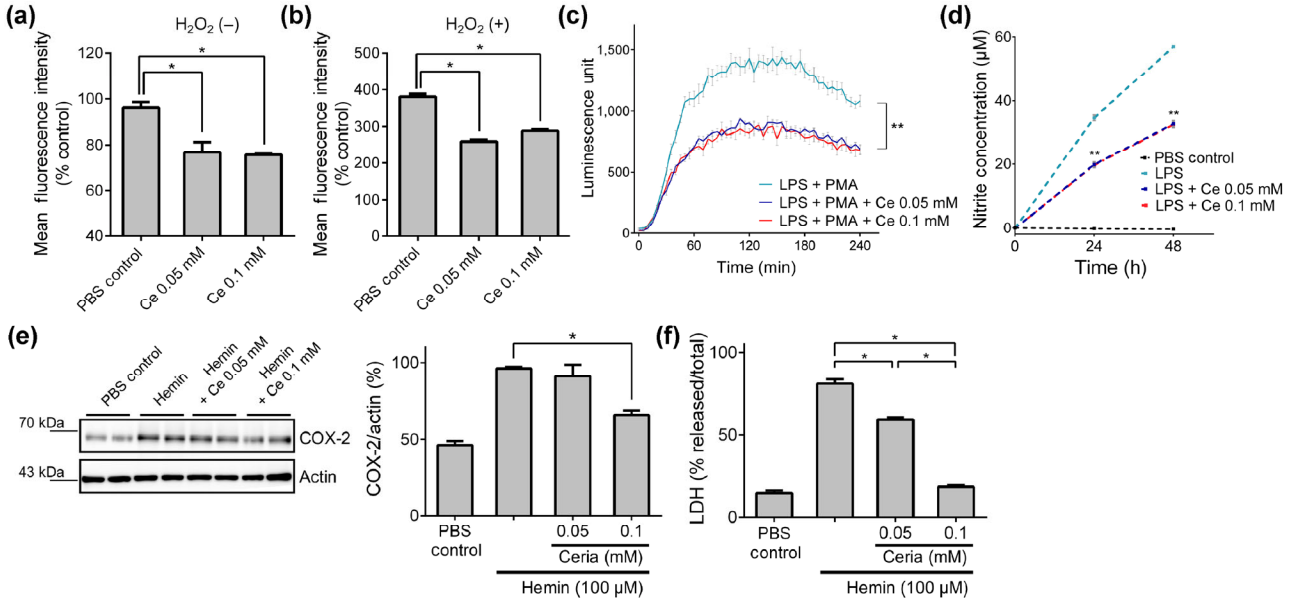

Figure 1 Anti-oxidative, anti-inflammatory, and cytoprotective effects of CeNPs *in vitro*. (a) and (b) DCF-DA assay. Mean fluorescence intensity in U937 cells measured by flow cytometry and expressed as a percentage of the untreated control group set as 100%. $n = 4$. (c) Superoxide anion assay. The luminescence intensities in U937 cells were obtained every 5 min for 4 h during the assay. $n = 4$. (d) NO assay. Quantification of NO_2^- concentrations at 0, 24, and 48 h after co-administration of CeNPs with LPS (1 μg/mL) to RAW264.7 cells as compared to the LPS-only group. $n = 4$. (e) Western blot analysis of COX-2 protein in RAW264.7 cells. Quantification of blots using the relative optical densities of COX-2 and β-actin protein. $n = 4$. (f) Quantification of LDH release in each group was expressed as a percentage of the positive control set as 100%. $n = 4$. Error bars, mean ± s.e.m. $^*P < 0.05$; $^{**}P < 0.01$.

2.9% vs. 96.2% ± 1.0%, $n = 4$, $P < 0.05$); however, 0.05 mM of CeNPs did not reduce COX-2 expression (Fig. 1(e)).

We carried out LDH and TUNEL assays to evaluate whether the anti-inflammatory effect of CeNPs could subsequently protect against hemin-induced cell death. In the LDH assay, in which LDH release was measured to quantify cell lysis indicating cell death, 80.8% ± 2.8% of total intracellular LDH was released after 6 h of hemin treatment. When the CeNPs were co-administered with 100 μM hemin for 6 h, LDH release showed a dose-dependent reduction (59.0% ± 1.4% at 0.05 mM, 18.3% ± 0.8% at 0.1 mM; $n = 4$, $P < 0.01$) (Fig. 1(f) and Table S2 in the ESM). In the TUNEL assay, terminal deoxynucleotidyl transferase labels DNA strand breaks during apoptosis [34], resulting in TUNEL positivity. The proportion of TUNEL-positive cells was reduced in a dose-dependent manner after treatment with the CeNPs (3.23% ± 0.04%, 2.42% ± 0.05%, and 1.35% ± 0.26% in the hemin only-, 0.05 mM CeNP-, and 0.1 mM CeNP-treated groups, respectively; $n = 4$, $P < 0.05$) (Fig. 2).

3.5 Tracking of intravenously injected RITC-CeNPs *in vivo*

There was no significant difference in any of the physiological parameters, including body weight, body temperature, serum glucose, and systolic and diastolic blood pressure, between the CeNPs-treated and control groups in all *in vivo* experiments (Table S3 in the ESM). After single injection of RITC-CeNPs, the RITC-CeNPs were mainly distributed in the perihematomal area, and few RITC-CeNPs were found in the contralateral hemisphere at 24 h after ICH induction (Figs. 3(a)–3(c)). The CeNPs were visualized under high power, and some of them were found to colocalize with DAPI (Figs. 3(d) and 3(e)). The RITC-CeNPs diffused throughout the interstitial space, but could not cross the ventricle or gray matter (Fig. 3(f)). The RITC-CeNPs clearly accumulated and the fluorescence signal was greatly increased in the perihematomal area in the ipsilateral hemisphere (Fig. 3(g)) according to the 3D reconstruction image. In the perihematomal area, the maximal fluorescence

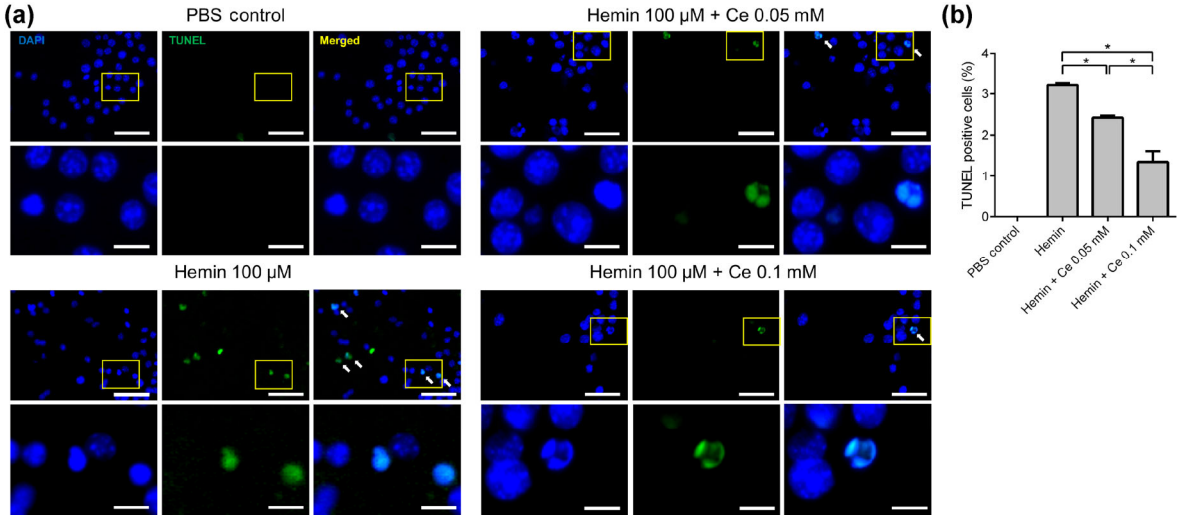

Figure 2 TUNEL assay in RAW264.7 cells *in vitro*. Cells of the positive control group were treated with hemin (100 μM) for 24 h, and CeNPs (0.05 or 0.1 mM) were co-administered in the experimental group. (a) Representative images show the presence of TUNEL-positive cells (green). Cells were counterstained with DAPI (blue). Arrows indicate TUNEL-positive cells. Scale bars, 40 μm in the first and third rows and 10 μm in the second and fourth rows. (b) Quantification of the proportion of TUNEL-positive cells. $n = 4$. Error bars, mean ± s.e.m. $^*P < 0.05$.

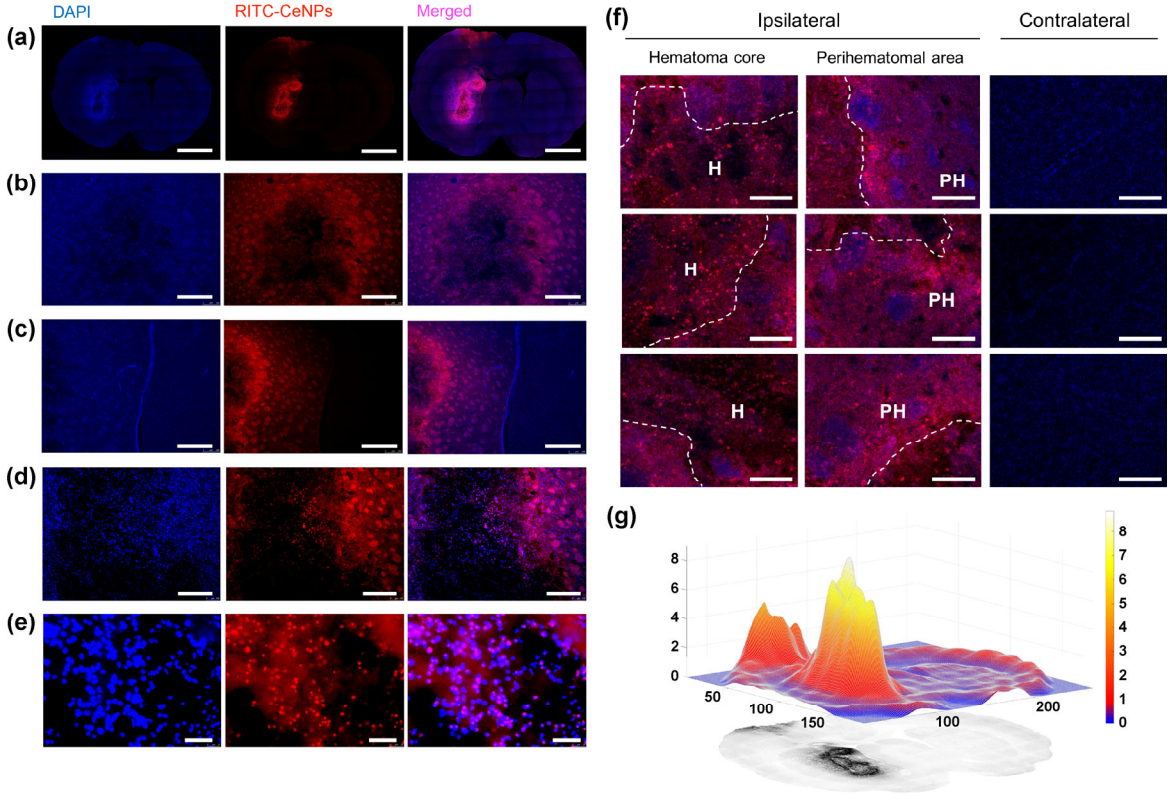

Figure 3 Distribution of CeNPs in the hemorrhagic brain. (a)–(e) Representative images showing the fluorescence of RITC-CeNPs (red) and DAPI (blue) under 561 and 340–380 nm light, respectively. RITC-CeNPs were distributed in both the intracellular and extracellular spaces. Scale bars, 3 mm (a), 500 μm (b) and (c), 250 μm (d), and 50 μm (e). (f) Distribution of the RITC-CeNPs in a representative plane. The fluorescence intensities of RITC-CeNPs were strong in the H and the PH, while the contralateral hemisphere showed weak red fluorescence. Scale bars, 100 μm. (g) Using computerized 3D reconstruction of fluorescence signals, signals for CeNPs were shown to greatly increase in the perihematomal area in the hemorrhagic hemisphere. Color bar, fold change of the mean fluorescence intensity.

intensity was 6.8-fold stronger than the mean fluorescence intensity, which was assumed to represent the relative density of CeNPs in the brain [35]. In addition, the mean fluorescence intensity in the ipsilateral hemisphere was 4.3 times stronger than that in the contralateral hemisphere.

3.6 Reduction of inflammatory activity and inflammatory cell recruitment by CeNPs

To evaluate the effects of CeNPs on the post-ICH inflammatory response, we investigated how CeNPs affected the number and the distribution of CD68-positive microglia/macrophages. A schematic diagram of the *in vivo* study protocols is provided in Fig. 4. To analyze each coronal brain section quantitatively, we semi-automatically counted the number of CD68-positive cells in the perihematomal area. The recruitment of CD68-positive inflammatory cells to the perihematomal area was decreased in the CeNP-treated group as compared to the control (2.12×10^4 cells/section vs. 2.97×10^4 cells/section, $n = 7$, $P < 0.05$, Figs. 5(a) and 5(b)). Furthermore, COX-2 expression in the ipsilateral hemisphere was significantly reduced in the CeNP-treated as compared to the control group (58.1% ± 5.3% vs. 91.4% ± 4.1%, $n = 4$, $P < 0.01$, Figs. 5(c) and 5(d)). In the dose-response analysis, CD68-positive cell counts were significantly decreased with dual (6 and 30 h) and triple (6, 30, and 54 h) doses

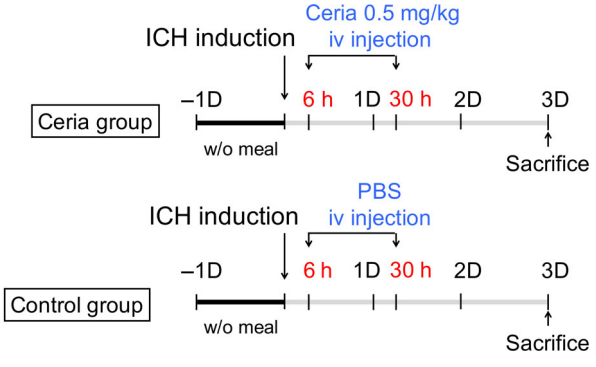

Figure 4 Schematic diagram of the study protocols in an *in vivo* ICH model. In 8-week-old male Sprague–Dawley rats, CeNPs or PBS were intravenously administered at 6 and 30 h after ICH induction. At 72 h, immunofluorescence staining and western blot analyses were conducted to confirm the anti-inflammatory effect of CeNPs, and the hematoma volume and brain water content were measured to confirm the reducing effect of CeNPs on hematoma volume and perihematomal edema.

compared with the control, but not with a single dose (Fig. S9(a) in the ESM).

3.7 Reduction of brain edema by CeNPs

The overall water content of the ipsilateral cerebral hemisphere, which was measured 72 h after ICH induction, was significantly decreased in the CeNPs-treated as compared to the PBS-injected group (79.90% ± 0.17% vs. 81.05% ± 0.33%, $n = 5$–6, $P < 0.01$, Fig. 6(a)). We calculated the relative water content increase, which is the difference in brain water content between the ipsilateral and contralateral hemispheres, for each animal. In contrast to the overall water content, which includes the intracellular, interstitial, and intravascular water contents, a water content increase implies pure brain edema. The relative water content increased by 1.74% ± 0.19% and 0.55% ± 0.29% in the control and CeNPs-treated groups, respectively (Fig. 6(b) and Table S4 in the ESM, *t*-test, $n = 5$–6, $P < 0.01$). Thus, our biocompatible custom-made CeNPs reduced perihematomal edema by 68.4% as compared to the control. In contrast, as expected, CeNP injection did not affect the hematoma volume itself (14.98 ± 5.56 mm^3 vs. 15.75 ± 4.31 mm^3, control and CeNP-treated groups, respectively, *t*-test, $n = 4$, Fig. 6(c) and Fig. S10 in the ESM) [36]. Furthermore, to adjust for variations in individual brain size, we calculated the hematoma volume relative to the contralateral hemisphere; no difference was found between the two groups (6.85% ± 1.33% vs. 6.76% ± 1.05% in the control and CeNP-treated groups, respectively, $n = 4$, Fig. 6(d)). In the dose-response analysis, brain water contents were significantly decreased with single (6 h), dual (6 and 30 h), and triple (6, 30, and 54 h) doses of CeNPs when compared to the control; however, there were no significant differences between the doses (Fig. S9(b) in the ESM).

3.8 Comparison between phospholipid-PEG vehicle and PEGylated CeNPs

To support the protective effects of CeNPs, we compared the effects of the phospholipid-PEG vehicle and CeNPs on inflammation and brain water content. Phospholipid-PEG micelle (vehicle) and RITC-conjugated vehicle had a mean hydrodynamic size of

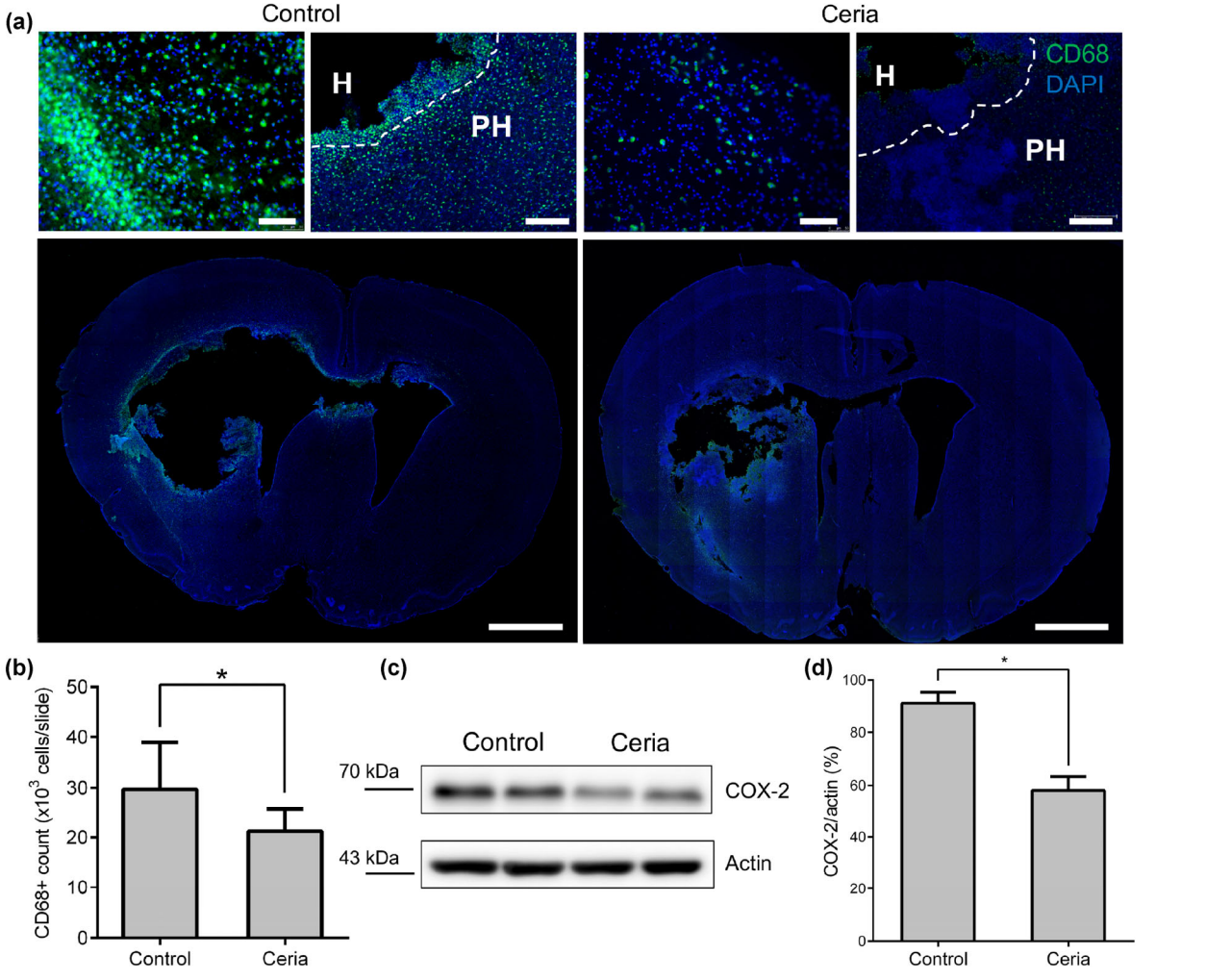

Figure 5 Anti-inflammatory effects of CeNPs in an *in vivo* intracerebral hemorrhage model. (a) The fluorescence intensities of CD68 (green) and DAPI (blue) were examined using a fluorescence microscope, and representative images are presented showing CD68-positive microglia/macrophages in the H and the PH. Scale bars, 50 μm, 200 μm, and 2 mm in each group. (b) Quantification of CD68-positive cells of entire sections, $n = 7$. (c) Western blot analysis of COX-2 protein in the ipsilateral hemisphere. (d) Quantification of blots shown in (c) using the relative optical densities of COX-2 and β-actin protein, $n = 4$. Error bars, mean ± s.e.m. $^*P < 0.05$.

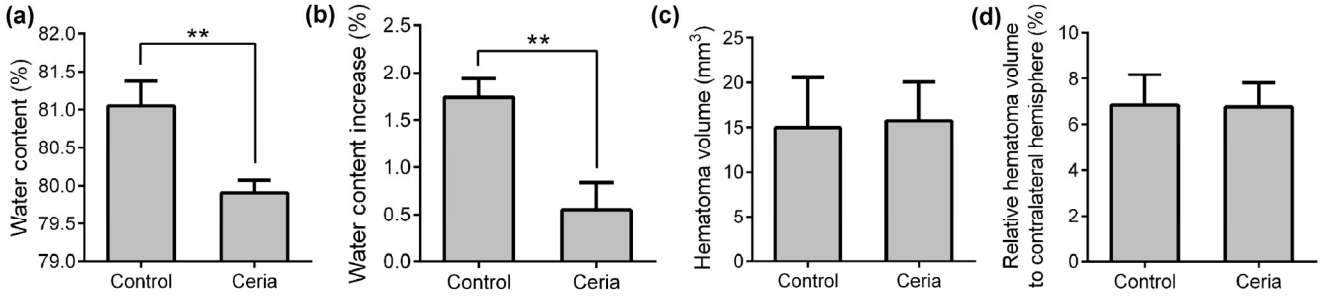

Figure 6 Measurement of brain water content and hematoma volume. (a) CeNPs (0.5 mg/kg) or an equal volume of PBS was intravenously administered twice at 6 and 30 h after induction of ICH, and the brains were harvested at 72 h after ICH induction. Overall brain water content was calculated after measuring the wet and dry weights of the ipsilateral hemisphere. $n = 5$–6. (b) The relative water content increase (%) was calculated by subtracting the water content of the contralateral hemisphere from that of the ipsilateral hemisphere. $n = 5$–6. (c) Measurement of hematoma volume. $n = 4$. (d) Measurement of relative hematoma volume to contralateral hemisphere. $n = 4$. Error bars, mean ± s.e.m. $^*P < 0.05$; $^{**}P < 0.01$.

1.3 and 11.8 nm, respectively. The intravenously injected RITC-conjugated vehicle was also well distributed in the perihematomal area, which was similar to the findings with RITC-CeNPs (Fig. 7(a)). The CeNPs reduced the recruitment of CD68-positive inflammatory cells to the perihematomal area as compared to the vehicle control (1.75×10^4 cells/section vs. 3.36×10^4 cells/section, $P < 0.05$, Fig. 7(b)). In addition, the CeNPs significantly reduced the relative water content increase when compared to the vehicle control (0.78% ± 0.21% vs. 1.40% ± 0.19%, $P < 0.05$, Fig. 7(c)).

4 Discussion

In this study, we synthesized small-sized, uniform, highly crystalline, and highly dispersed PEGylated CeNPs. We found that our custom CeNPs reduced ROS and reactive nitrogen species (RNS), and inhibited hemin-induced COX-2 expression and cell death in macrophages. In the collagenase-induced rodent ICH model, the CeNPs were mainly located in the perihematomal area after intravenous administration. The number of CD68-positive microglia/macrophages decreased in the perihematomal area in the CeNP-treated group, and COX-2 expression was reduced. Finally, our custom CeNPs reduced the relative brain water content, which reflects perihematomal edema, by 68.4% as compared to the control.

CeNPs are known for their free radical scavenging activity. The alternation between the two cerium oxidation states (Ce^{3+} and Ce^{4+}) is the origin of the potent ROS scavenging activity of CeNPs [37]. Moreover, CeNPs can act as biological anti-oxidants owing to their superoxide dismutase- and catalase-mimetic activities [38]. However, CeNPs must be biocompatible and non-toxic for biomedical applications, because safety is crucial for therapeutic agents to be used in humans. Commercially available CeNPs are not suitable for use *in vivo*, as several safety issues remain unresolved.

A high dose of CeNPs induces inflammation in organs, suggesting their potentially harmful effects [39]. Thus, we aimed to synthesize custom CeNPs that are biocompatible and safe for human applications. Our custom CeNPs were highly dispersed, with little agglomeration, as previously described [21]. In the DCF-DA assay, our custom CeNPs reduced the level of endogenous ROS when administered to unstimulated macrophages. This result is different from the results of previous studies, which showed that CeNPs could induce oxidative stress in other cell types such as cancer cells or lung epithelial cells [40, 41].

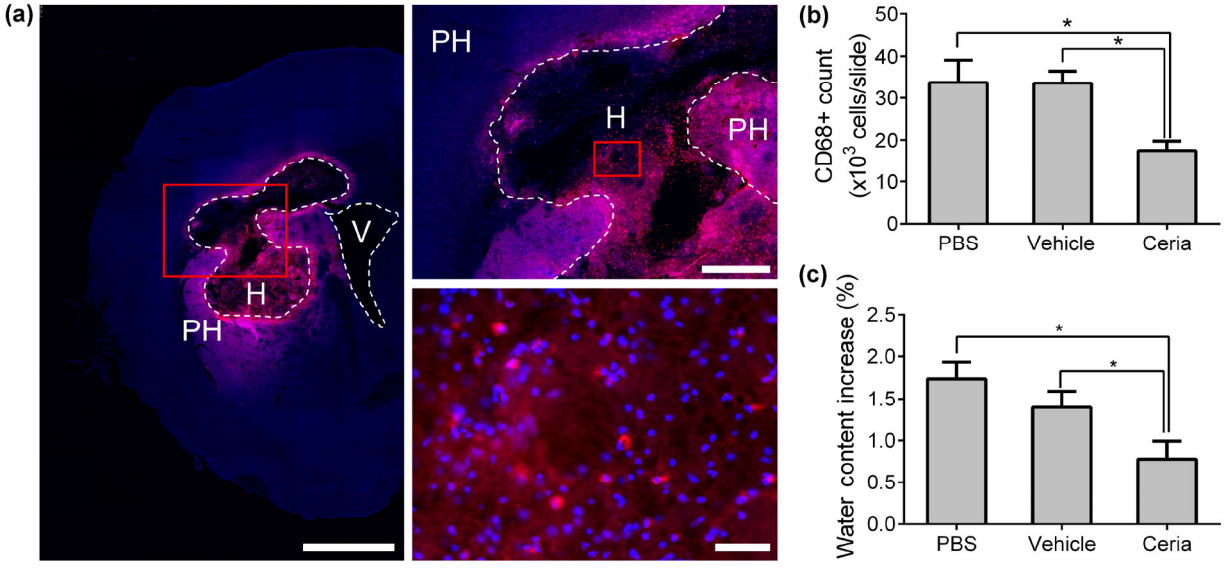

Figure 7 *In vivo* experiments with phospholipid-PEG micelle vehicle. (a) Representative images showing the fluorescence of RITC-vehicle (red) and DAPI (blue) under 561 and 340–380 nm light, respectively. Scale bars, 2 mm (left), 500 μm (upper), and 50 μm (bottom). (b) Quantification of the number of CD68-positive cells of entire perihematomal area per sections. $n = 4$. (c) The relative water content increase (%) was measured in the PBS-, vehicle-, and CeNP-treated groups. $n = 5$. Error bars, mean ± s.e.m. *$P < 0.05$.

From a pathophysiological perspective, the hematoma is formed by extravasated blood and expands in a few hours [42]. Initially, this causes physical disruption of the neurovascular structures around the hematoma. Later, cytotoxic molecules in the extravasated blood, such as damage-associated molecular patterns, impose a strong cytotoxic and pro-oxidative insult [7]. Heme, the major component of hemoglobin, is the major source of intracellular ROS in ICH [43]. Heme is degraded by heme oxygenase into carbon monoxide, biliverdin, and iron [44]. Intracellular ferrous iron (Fe^{2+}) can catalyze the transformation of hydrogen peroxide to the hydroxyl radical, which is a dangerous and reactive form of ROS [45]. These intracellular ROS can damage various molecules such as DNA, lipids, and amino acids. Furthermore, ROS act as intracellular signals and affect gene expression as well as some redox-sensitive signaling pathways [46].

During post-ICH inflammation, the nuclear factor-kappa B (NF-κB) signaling pathway is activated mainly in resident microglia and infiltrating macrophages. Inducible nitric oxide synthase (iNOS) protein, which acts downstream of NF-κB, is subsequently expressed. ICH-induced iNOS protein expression persists until 3 to 7 days after ICH [47]. The exact mechanism by which ROS stimulate iNOS expression has not been fully elucidated, but studies have shown that ROS play an important role in iNOS protein activation [48]. Under normal physiological conditions, NO acts as a mediator of neurotransmission, neuronal survival, proliferation, and differentiation. However, under pathological conditions, excessive NO causes oxidative stress in the form of peroxynitrite, which is produced by the reaction between NO and O_2^- [49]. We found that the CeNPs consistently reduced NO over time, suggesting that they could attenuate the later steps of the inflammatory reaction as well as directly reduce RNS and peroxynitrites. Oxidative stress, which plays a key role in post-ICH inflammation, can be a predictor of poor clinical outcome in ICH patients [50]. ROS can evoke inflammation by themselves or can be produced during inflammatory processes for signal transduction [51, 52]. There are several sources of ROS in ICH, including mitochondrial dysfunction, hemoglobin-heme-iron (Hb-heme-iron), and inflammatory cells such as microglia/macrophages. Hb-heme-iron, hemoglobin and its degradation derivatives, is most abundant in the extracellular space in the clinical setting of ICH. Accumulating evidence shows that Hb-heme-iron mainly induces oxidative stress [53]. Haptoglobin, an acute-phase response protein that neutralizes hemoglobin, can inhibit the neuronal damage in ICH [54]. Deferoxamine, an iron chelator, has also been shown to attenuate brain edema and neurological deficits in a rat ICH model [55]. For this reason, hemin was used as an *in vitro* proxy for the ICH model in this study. Hemin (ferriprotoporphyrin IX chloride), an oxidized form of the heme moiety of hemoglobin, has cytotoxicity through free-radical generation, and can lead to ICH-induced inflammation by activating microglia/macrophages [56].

We demonstrated that the CeNPs significantly reduced hemin-induced COX-2 expression at higher dose. COX-2 is an inducible enzyme that increases after exposure to inflammatory stimuli and brain insult [57]. ROS may play an important role in mediating the hemin-induced inflammation and COX-2 signaling pathway in various organs [58]. COX-2 has a major role in mediating inflammatory responses and the interaction between neurons, microglia, and endothelial cells after ICH, augmenting brain injury [59]. Furthermore, the results of our *in vitro* LDH and TUNEL assays demonstrated that CeNPs remarkably reduced hemin-induced cell death in macrophages. ICH causes a wide range of tissue damage in the perihematomal area composed of neurons, astrocytes, endothelial cells, and microglia/macrophages. Macrophage cell death *per se* could act as a proinflammatory signal with various cytokines, worsening brain damage [60]. Heme can induce macrophage necrosis through ROS and autocrine tumor necrosis factor [61]. Thus, these findings suggest that CeNPs can prevent macrophage necrosis, which exacerbates inflammatory cascades via ROS scavenging. ROS/RNS have a direct influence on cell death signaling pathways and oxidize intracellular lipids, proteins, or nucleic acids [62]. There are three ROS-mediated cell death pathways: PI3K/Akt, MAPK/P38, and NF-κB [53]. Cytochrome c–mediated apoptosis is also important in relation to mitochondrial function [63]. Although the determination of the specific involvement of all of these pathways in the context of ICH requires further research, ROS

possibly influence the cell death pathways at multiple stages. Interestingly, although a ceiling effect occurred at lower dose of CeNPs in the assays for ROS/RNS, CeNPs were effective at higher doses in reducing inflammatory cell death. These findings suggest that CeNPs have additional effects against inflammation or pyroptotic cell death with more complex mechanisms, which could not be simply explained by their anti-ROS/RNS effects [64]. Taken together, our *in vitro* experiments showed that CeNPs may play an important role in deciding the fate of macrophages through ROS/RNS scavenging and their additional effects on inflammatory pathway at the higher dose.

Delivery of nanoparticles to the target area is a critical issue in the treatment of various diseases. Delivering therapeutic agents into the brain is especially difficult, because the blood–brain barrier (BBB) tightly sequestrates the brain from the blood circulation [65]. It is very interesting that most of the RITC-CeNPs were largely distributed in the perihematomal area, but not in the intact brain tissue, after intravenous injection. This finding indicates that circulating CeNPs can penetrate only the damaged BBB in the perihematomal area. After initial hemorrhage, a prominent inflammatory response occurs, with activation of resident microglia and recruitment of macrophages. Leukocyte-derived ROS, pro-inflammatory cytokines, and chemokines accelerate disruption of the BBB and surrounding tissues [66]. Specifically, CD68-positive cells, which originate from the activation of circulating monocytes and their transformation into macrophages, play major roles in the initial inflammatory response. A recent study showed that CD68-positive cells increased in the perihematomal area adjacent to the hemorrhage [67]. COX-2 also affects pathological processes by vasodilatation and increasing vascular permeability [57], thus contributing to perihematomal edema formation. Indeed, COX-2 inhibitors are known to reduce perihematomal edema via suppressing COX-2 activity in ICH [68]. In this study, protein expression of COX-2 was reduced in both the *in vitro* and *in vivo* ICH models, suggesting that CeNPs affect COX-2-related inflammatory pathways. As most CeNPs were located in the perihematomal area in our experiment, this suggests that the CeNPs scavenge ROS *in situ* with a self-regenerative property and reduce inflammation and cell death by affecting inflammatory cascades. Activated microglia and macrophages may be major cell types uptaking CeNPs, because a large number of macrophages from the bloodstream infiltrate into the perihematomal area, and the activated microglia/macrophages vigorously phagocytose extracellular particles [22]. Since activated microglia/macrophages play an essential role in post-ICH inflammation, we speculate that our CeNPs mainly modulate these cell types in the *in vivo* ICH model. Taken together, our *in vitro* and *in vivo* results suggest that CeNPs may reduce post-ICH brain injury via anti-ROS/RNS, anti-inflammatory, or more complex and systemic mechanisms.

The CeNPs did not reduce the volume of the hematoma itself, but they significantly reduced the brain edema. In the collagenase-induced rodent ICH model, a hematoma is produced by the disruption of the blood vessels and leakage of blood into the brain parenchyma. Collagenase is known to produce and increase the hematoma rapidly during the first few hours [36], and the subsequent brain edema forms in two phases. In the first phase of the first several hours, plasma leaks through endothelial cells due to hydrostatic pressure, resulting in a vasogenic edema [69]. In the second phase of the first 2–3 days, a coagulation cascade is activated and exacerbates the brain edema. Thrombin is an essential component in the clotting cascade and acts as a potent edema producer. Thrombin also has direct neurotoxicity that causes inflammation, seizure, and reactive gliosis, resulting in cytotoxic edema and neuronal apoptosis [70]. In addition, hemoglobin and its degradation products play a major role in edema formation [29]. In human patients, perihematomal edema peaks at approximately 3 days, and neurological deterioration often occurs during this phase. Heme is degraded by heme oxygenase into iron, carbon monoxide, and biliverdin. The overload of iron generates abundant free radicals and results in further BBB disruption [71]. The timing of brain edema formation overlaps with the acute inflammatory phase. Thus, reducing brain edema via attenuating inflammation after ICH is generally considered as an important goal of ICH treatment [72].

A few points may require further clarification. First,

as there were discrepancies in the effects of CeNPs in various *in vitro* assays, the dose-response relationship is currently not clear at the concentrations tested in the present study. Second, the long-term safety and clearance of CeNPs from the brain should be examined in future studies before application in patients. Third, sex differences in the efficacy of CeNPs were not examined in this study. Interactions between sex, age, and underlying disease on the outcome of CeNP treatment should be tested in future research. Fourth, although we used PBS as a control to evaluate the overall effect of the CeNPs compared to that of placebo, CeNPs also demonstrated protective effects in the experiments using phospholipid-PEG micelles as a vehicle control.

5 Conclusions

In conclusion, our study revealed that CeNPs can reduce secondary brain injury in ICH. The CeNPs significantly reduced perihematomal edema formation by attenuating oxidative injury and inflammation. The CeNPs were largely recruited to the perihematomal area, where they could exert a maximum protective effect. Our custom CeNPs passed through the damaged BBB, which would enable targeted therapy for ICH and reduce inappropriate delivery to intact tissues. Our biocompatible custom CeNPs are uniform, highly crystalline, PEGylated, and show low agglomeration, making them superior to commercialized CeNPs in terms of efficacy and safety. These biocompatible nanoparticles are more likely to react with free radicals because of their small core size and good colloidal stability. PEGylated CeNPs have a long circulation time, and are thus efficiently recruited to the hemorrhagic brain. To our knowledge, this is the first report to demonstrate the protective effects of CeNPs in ICH, offering hope for patients with ICH with a potentially novel therapeutic agent.

Acknowledgements

This work was supported by grants of the followings: The Korea Health Technology R&D Project through the Korea Health Industry Development Institute (KHIDI), the Ministry of Health & Welfare, Republic of Korea (No. HI14C0211), Basic Science Research Program through the National Research Foundation of Korea (NRF) funded by the Ministry of Science, ICT & Future Planning (No. NRF-2015R1A2A2A 01007770), and the Institute for Basic Science (IBS), Republic of Korea (No. IBS-R006-D1).

Electronic Supplementary Material: Supplementary material (schematic diagram of the study protocol, supporting images of the methods, detailed characteristics of the CeNPs and the vehicles, supporting *in vivo* experiments, and the detailed results of LDH assay and brain water content measurement) is available in the online version of this article at http://dx.doi.org/10.1007/s12274-017-1478-6.

References

[1] Qureshi, A. I.; Tuhrim, S.; Broderick, J. P.; Batjer, H. H.; Hondo, H.; Hanley, D. F. Spontaneous intracerebral hemorrhage. *N. Engl. J. Med.* **2001**, *344*, 1450–1460.

[2] Labovitz, D. L.; Halim, A.; Boden-Albala, B.; Hauser, W. A.; Sacco, R. L. The incidence of deep and lobar intracerebral hemorrhage in whites, blacks, and Hispanics. *Neurology* **2005**, *65*, 518–522.

[3] Qureshi, A. I.; Mendelow, A. D.; Hanley, D. F. Intracerebral haemorrhage. *Lancet* **2009**, *373*, 1632–1644.

[4] Hemphill, J. C.; Greenberg, S. M.; Anderson, C. S.; Becker, K.; Bendok, B. R.; Cushman, M.; Fung, G. L.; Goldstein, J. N.; Macdonald, R. L.; Mitchell, P. H. et al. Guidelines for the management of spontaneous intracerebral hemorrhage: A guideline for healthcare professionals from the American heart association/American stroke association. *Stroke* **2015**, *46*, 2032–2060.

[5] Mendelow, A. D.; Gregson, B. A.; Fernandes, H. M.; Murray, G. D.; Teasdale, G. M.; Hope, D. T.; Karimi, A.; Shaw, M. D. M.; Barer, D. H. Early surgery versus initial conservative treatment in patients with spontaneous supratentorial intracerebral haematomas in the International Surgical Trial in Intracerebral Haemorrhage (STICH): A randomised trial. *Lancet* **2005**, *365*, 387–397.

[6] Mayer, S. A.; Brun, N. C.; Begtrup, K.; Broderick, J.; Davis, S.; Diringer, M. N.; Skolnick, B. E.; Steiner, T. Efficacy and safety of recombinant activated factor VII for acute intracerebral hemorrhage. *N. Engl. J. Med.* **2008**, *358*, 2127–2137.

[7] Aronowski, J.; Zhao, X. R. Molecular pathophysiology of cerebral hemorrhage: Secondary brain injury. *Stroke* **2011**, *42*, 1781–1786.

[8] Masada, T.; Hua, Y.; Xi, G. H.; Yang, G. Y.; Hoff, J. T.; Keep, R. F. Attenuation of intracerebral hemorrhage and thrombin-induced brain edema by overexpression of interleukin-1 receptor antagonist. *J. Neurosurg.* **2001**, *95*, 680–686.

[9] Hua, Y.; Keep, R. F.; Hoff, J. T.; Xi, G. H. Brain injury after intracerebral hemorrhage: The role of thrombin and iron. *Stroke* **2007**, *38*, 759–762.

[10] Keep, R. F.; Hua, Y.; Xi, G. H. Intracerebral haemorrhage: Mechanisms of injury and therapeutic targets. *Lancet Neurol.* **2012**, *11*, 720–731.

[11] Dahle, J. T.; Arai, Y. Environmental geochemistry of cerium: Applications and toxicology of cerium oxide nanoparticles. *Int. J. Environ. Res. Public Health* **2015**, *12*, 1253–1278.

[12] Chen, J. P.; Patil, S.; Seal, S.; McGinnis, J. F. Rare earth nanoparticles prevent retinal degeneration induced by intracellular peroxides. *Nat. Nanotechnol.* **2006**, *1*, 142–150.

[13] Das, M.; Patil, S.; Bhargava, N.; Kang, J.-F.; Riedel, L. M.; Seal, S.; Hickman, J. J. Auto-catalytic ceria nanoparticles offer neuroprotection to adult rat spinal cord neurons. *Biomaterials* **2007**, *28*, 1918–1925.

[14] Chen, S. Z.; Hou, Y. J.; Cheng, G.; Zhang, C. M.; Wang, S. X.; Zhang, J. C. Cerium oxide nanoparticles protect endothelial cells from apoptosis induced by oxidative stress. *Biol. Trace Elem. Res.* **2013**, *154*, 156–166.

[15] Dowding, J. M.; Das, S.; Kumar, A.; Dosani, T.; McCormack, R.; Gupta, A.; Sayle, T. X. T.; Sayle, D. C.; von Kalm, L.; Seal, S. et al. Cellular interaction and toxicity depend on physicochemical properties and surface modification of redox-active nanomaterials. *ACS Nano* **2013**, *7*, 4855–4868.

[16] Selvaraj, V.; Nepal, N.; Rogers, S.; Manne, N. D. P. K.; Arvapalli, R.; Rice, K. M.; Asano, S.; Fankhanel, E.; Ma, J. J.; Shokuhfar, T. et al. Inhibition of MAP kinase/NF-kB mediated signaling and attenuation of lipopolysaccharide induced severe sepsis by cerium oxide nanoparticles. *Biomaterials* **2015**, *59*, 160–171.

[17] Hirst, S. M.; Karakoti, A. S.; Tyler, R. D.; Sriranganathan, N.; Seal, S.; Reilly, C. M. Anti-inflammatory properties of cerium oxide nanoparticles. *Small* **2009**, *5*, 2848–2856.

[18] Manne, N. D.; Arvapalli, R.; Nepal, N.; Thulluri, S.; Selvaraj, V.; Shokuhfar, T.; He, K.; Rice, K. M.; Asano, S.; Maheshwari, M. et al. Therapeutic potential of cerium oxide nanoparticles for the treatment of peritonitis induced by polymicrobial insult in Sprague–Dawley rats. *Crit. Care Med.* **2015**, *43*, e477–e489.

[19] Manne, N. D. P. K.; Arvapalli, R.; Nepal, N.; Shokuhfar, T.; Rice, K. M.; Asano, S.; Blough, E. R. Cerium oxide nanoparticles attenuate acute kidney injury induced by intra-abdominal infection in Sprague–Dawley rats. *J. Nanobiotechnology* **2015**, *13*, 75.

[20] Kyosseva, S. V.; Chen, L. J.; Seal, S.; McGinnis, J. F. Nanoceria inhibit expression of genes associated with inflammation and angiogenesis in the retina of Vldlr null mice. *Exp. Eye Res.* **2013**, *116*, 63–74.

[21] Kim, C. K.; Kim, T.; Choi, I. Y.; Soh, M.; Kim, D.; Kim, Y. J.; Jang, H.; Yang, H. S.; Kim, J. Y.; Park, H. K. et al. Ceria nanoparticles that can protect against ischemic stroke. *Angew. Chem., Int. Ed.* **2012**, *51*, 11039–11043.

[22] Mracsko, E.; Veltkamp, R. Neuroinflammation after intracerebral hemorrhage. *Front. Cell. Neurosci.* **2014**, *8*, 388.

[23] Chao, C. C.; Hu, S. X.; Sheng, W. S.; Bu, D. F.; Bukrinsky, M. I.; Peterson, P. K. Cytokine-stimulated astrocytes damage human neurons via a nitric oxide mechanism. *Glia* **1996**, *16*, 276–284.

[24] Sinensky, M. C.; Leiser, A. L.; Babich, H. Oxidative stress aspects of the cytotoxicity of carbamide peroxide: *In vitro* studies. *Toxicol. Lett.* **1995**, *75*, 101–109.

[25] Grossetete, M.; Rosenberg, G. A. Matrix metalloproteinase inhibition facilitates cell death in intracerebral hemorrhage in mouse. *J. Cereb. Blood Flow Metab.* **2008**, *28*, 752–763.

[26] Aguilar, M. I.; Brott, T. G. Update in intracerebral hemorrhage. *Neurohospitalist* **2011**, *1*, 148–159.

[27] Kim, C. K.; Ryu, W. S.; Choi, I. Y.; Kim, Y. J.; Rim, D.; Kim, B. J.; Jang, H.; Yoon, B. W.; Lee, S. H. Detrimental effects of leptin on intracerebral hemorrhage via the STAT3 signal pathway. *J. Cereb. Blood Flow Metab.* **2013**, *33*, 944–953.

[28] Jung, K. H.; Chu, K.; Jeong, S. W.; Han, S. Y.; Lee, S. T.; Kim, J. Y.; Kim, M.; Roh, J. K. HMG-CoA reductase inhibitor, atorvastatin, promotes sensorimotor recovery, suppressing acute inflammatory reaction after experimental intracerebral hemorrhage. *Stroke* **2004**, *35*, 1744–1749.

[29] Huang, F.-P.; Xi, G. H.; Keep, R. F.; Hua, Y.; Nemoianu, A.; Hoff, J. T. Brain edema after experimental intracerebral hemorrhage: Role of hemoglobin degradation products. *J. Neurosurg.* **2002**, *96*, 287–293.

[30] Crow, J. P. Dichlorodihydrofluorescein and dihydrorhodamine 123 are sensitive indicators of peroxynitrite *in vitro*: Implications for intracellular measurement of reactive nitrogen and oxygen species. *Nitric Oxide* **1997**, *1*, 145–157.

[31] Grisham, M. B.; Jourd'Heuil, D.; Wink, D. A. Nitric oxide. I. Physiological chemistry of nitric oxide and its metabolites: Implications in inflammation. *Am. J. Physiol.* **1999**, *276*, G315–G321.

[32] Laird, M. D.; Wakade, C.; Alleyne, C. H., Jr.; Dhandapani,

K. M. Hemin-induced necroptosis involves glutathione depletion in mouse astrocytes. *Free Radic. Biol. Med.* **2008**, *45*, 1103–1114.

[33] Mitchell, J. A.; Warner, T. D. Cyclo-oxygenase-2: Pharmacology, physiology, biochemistry and relevance to NSAID therapy. *Br. J. Pharmacol.* **1999**, *128*, 1121–1132.

[34] Gavrieli, Y.; Sherman, Y.; Ben-Sasson, S. A. Identification of programmed cell death *in situ* via specific labeling of nuclear DNA fragmentation. *J. Cell Biol.* **1992**, *119*, 493–501.

[35] Ljosa, V.; Carpenter, A. E. Introduction to the quantitative analysis of two-dimensional fluorescence microscopy images for cell-based screening. *PLoS Comput. Biol.* **2009**, *5*, e1000603.

[36] MacLellan, C. L.; Silasi, G.; Poon, C. C.; Edmundson, C. L.; Buist, R.; Peeling, J.; Colbourne, F. Intracerebral hemorrhage models in rat: Comparing collagenase to blood infusion. *J. Cereb. Blood Flow Metab.* **2008**, *28*, 516–525.

[37] Karakoti, A. S.; Kuchibhatla, S. V. N. T.; Babu, K. S.; Seal, S. Direct synthesis of nanoceria in aqueous polyhydroxyl solutions. *J. Phys. Chem. C* **2007**, *111*, 17232–17240.

[38] Karakoti, A. S.; Monteiro-Riviere, N. A.; Aggarwal, R.; Davis, J. P.; Narayan, R. J.; Self, W. T.; McGinnis, J.; Seal, S. Nanoceria as antioxidant: Synthesis and biomedical applications. *JOM* **2008**, *60*, 33–37.

[39] Poma, A.; Ragnelli, A. M.; de Lapuente, J.; Ramos, D.; Borras, M.; Aimola, P.; Di Gioacchino, M.; Santucci, S.; De Marzi, L. *In vivo* inflammatory effects of ceria nanoparticles on CD-1 mouse: Evaluation by hematological, histological, and TEM analysis. *J. Immunol. Res.* **2014**, *2014*, 361419.

[40] Alili, L.; Sack, M.; von Montfort, C.; Giri, S.; Das, S.; Carroll, K. S.; Zanger, K.; Seal, S.; Brenneisen, P. Downregulation of tumor growth and invasion by redox-active nanoparticles. *Antioxid. Redox Signal.* **2013**, *19*, 765–778.

[41] Park, E.-J.; Choi, J.; Park, Y.-K.; Park, K. Oxidative stress induced by cerium oxide nanoparticles in cultured BEAS-2B cells. *Toxicology* **2008**, *245*, 90–100.

[42] Kazui, S.; Naritomi, H.; Yamamoto, H.; Sawada, T.; Yamaguchi, T. Enlargement of spontaneous intracerebral hemorrhage: Incidence and time course. *Stroke* **1996**, *27*, 1783–1787.

[43] Goldstein, L.; Teng, Z. P.; Zeserson, E.; Patel, M.; Regan, R. F. Hemin induces an iron-dependent, oxidative injury to human neuron-like cells. *J Neurosci. Res.* **2003**, *73*, 113–121.

[44] Wagner, K. R.; Sharp, F. R.; Ardizzone, T. D.; Lu, A. G.; Clark, J. F. Heme and iron metabolism: Role in cerebral hemorrhage. *J. Cereb. Blood Flow Metab.* **2003**, *23*, 629–652.

[45] Kress, G. J.; Dineley, K. E.; Reynolds, I. J. The relationship between intracellular free iron and cell injury in cultured neurons, astrocytes, and oligodendrocytes. *J. Neurosci.* **2002**, *22*, 5848–5855.

[46] Barbieri, S. S.; Eligini, S.; Brambilla, M.; Tremoli, E.; Colli, S. Reactive oxygen species mediate cyclooxygenase-2 induction during monocyte to macrophage differentiation: Critical role of NADPH oxidase. *Cardiovasc. Res.* **2003**, *60*, 187–197.

[47] Campuzano, O.; Castillo-Ruiz, M. M.; Acarin, L.; Castellano, B.; Gonzalez, B. Distinct pattern of microglial response, cyclooxygenase-2, and inducible nitric oxide synthase expression in the aged rat brain after excitotoxic damage. *J. Neurosci. Res.* **2008**, *86*, 3170–3183.

[48] Meyer, M.; Schreck, R.; Baeuerle, P. A. H_2O_2 and antioxidants have opposite effects on activation of NF-kappa B and AP-1 in intact cells: AP-1 as secondary antioxidant-responsive factor. *EMBO J.* **1993**, *12*, 2005–2015.

[49] Ding, R.; Chen, Y. Z.; Yang, S.; Deng, X. Q.; Fu, Z. H.; Feng, L.; Cai, Y. Q.; Du, M. X.; Zhou, Y. X.; Tang, Y. P. Blood-brain barrier disruption induced by hemoglobin *in vivo*: Involvement of up-regulation of nitric oxide synthase and peroxynitrite formation. *Brain Res.* **2014**, *1571*, 25–38.

[50] Wagner, K. R.; Packard, B. A.; Hall, C. L.; Smulian, A. G.; Linke, M. J.; de Courten-Myers, G. M.; Packard, L. M.; Hall, N. C. Protein oxidation and heme oxygenase-1 induction in porcine white matter following intracerebral infusions of whole blood or plasma. *Dev. Neurosci.* **2002**, *24*, 154–160.

[51] Mittal, M.; Siddiqui, M. R.; Tran, K.; Reddy, S. P.; Malik, A. B. Reactive oxygen species in inflammation and tissue injury. *Antioxid. Redox Sign.* **2014**, *20*, 1126–1167.

[52] Selvaraj, V.; Manne, N. D.; Arvapalli, R.; Rice, K. M.; Nandyala, G.; Fankenhanel, E.; Blough, E. R. Effect of cerium oxide nanoparticles on sepsis induced mortality and NF-κB signaling in cultured macrophages. *Nanomedicine* **2015**, *10*, 1275–1288.

[53] Hu, X.; Tao, C. Y.; Gan, Q.; Zheng, J.; Li, H.; You, C. Oxidative stress in intracerebral hemorrhage: Sources, mechanisms, and therapeutic targets. *Oxid. Med. Cell. Longev.* **2016**, *2016*, 3215391.

[54] Zhao, X. R.; Song, S.; Sun, G. H.; Strong, R.; Zhang, J.; Grotta, J. C.; Aronowski, J. Neuroprotective role of haptoglobin after intracerebral hemorrhage. *J. Neurosci.* **2009**, *29*, 15819–15827.

[55] Nakamura, T.; Keep, R. F.; Hua, Y.; Schallert, T.; Hoff, J. T.; Xi, G. H. Deferoxamine-induced attenuation of brain edema and neurological deficits in a rat model of intracerebral hemorrhage. *J. Neurosurg.* **2004**, *100*, 672–678.

[56] Lin, S.; Yin, Q.; Zhong, Q.; Lv, F.-L.; Zhou, Y.; Li, J.-Q.; Wang, J.-Z.; Su, B. Y.; Yang, Q.-W. Heme activates TLR4-mediated inflammatory injury via MyD88/TRIF signaling pathway in intracerebral hemorrhage. *J. Neuroinflamm.* **2012**, *9*, 46.

[57] Gong, C.; Ennis, S. R.; Hoff, J. T.; Keep, R. F. Inducible cyclooxygenase-2 expression after experimental intracerebral hemorrhage. *Brain Res.* **2001**, *901*, 38–46.

[58] Wu, B.; Chen, X. H.; He, B.; Liu, S. Y.; Li, Y. F.; Wang, Q. X.; Gao, H. J.; Wang, S. F.; Liu, J. B.; Zhang, S. C. et al. ROS are critical for endometrial breakdown via NF-κB–COX-2 signaling in a female mouse menstrual-like model. *Endocrinology* **2014**, *155*, 3638–3648.

[59] Zhao, X. R.; Zhang, Y. J.; Strong, R.; Zhang, J.; Grotta, J. C.; Aronowski, J. Distinct patterns of intracerebral hemorrhage-induced alterations in NF-κB subunit, iNOS, and COX-2 expression. *J. Neurochem.* **2007**, *101*, 652–663.

[60] Taylor, R. A.; Sansing, L. H. Microglial responses after ischemic stroke and intracerebral hemorrhage. *Clin. Dev. Immunol.* **2013**, *2013*, 746068.

[61] Fortes, G. B.; Alves, L. S.; de Oliveira, R.; Dutra, F. F.; Rodrigues, D.; Fernandez, P. L.; Souto-Padron, T.; De Rosa, M. J.; Kelliher, M.; Golenbock, D. et al. Heme induces programmed necrosis on macrophages through autocrine TNF and ROS production. *Blood* **2012**, *119*, 2368–2375.

[62] Fleury, C.; Mignotte, B.; Vayssière, J.-L. Mitochondrial reactive oxygen species in cell death signaling. *Biochimie* **2002**, *84*, 131–141.

[63] Orrenius, S. Reactive oxygen species in mitochondria-mediated cell death. *Drug Metab. Rev.* **2007**, *39*, 443–455.

[64] Bergsbaken, T.; Fink, S. L.; Cookson, B. T. Pyroptosis: Host cell death and inflammation. *Nat. Rev. Microbiol.* **2009**, *7*, 99–109.

[65] Lockman, P. R.; Mumper, R. J.; Khan, M. A.; Allen, D. D. Nanoparticle technology for drug delivery across the blood-brain barrier. *Drug Dev. Ind. Pharm.* **2002**, *28*, 1–13.

[66] Wang, J. Preclinical and clinical research on inflammation after intracerebral hemorrhage. *Prog. Neurobiol.* **2010**, *92*, 463–477.

[67] Dahnovici, R. M.; Pintea, I. L.; Mălăescu, D. G.; Busuioc, C. J.; Predescu, A.; Mogoantă, L. Microscopic aspects of macrophage system cells in hemorrhagic stroke in humans. *Rom. J. Morphol. Embryol.* **2011**, *52*, 1249–1253.

[68] Chu, K.; Jeong, S. W.; Jung, K. H.; Han, S. Y.; Lee, S. T.; Kim, M.; Roh, J. K. Celecoxib induces functional recovery after intracerebral hemorrhage with reduction of brain edema and perihematomal cell death. *J. Cereb. Blood Flow Metab.* **2004**, *24*, 926–933.

[69] Xi, G. H.; Wagner, K. R.; Keep, R. F.; Hua, Y.; de Courten-Myers, G. M.; Broderick, J. P.; Brott, T. G.; Hoff, J. T.; Muizelaar, J. P. Role of blood clot formation on early edema development after experimental intracerebral hemorrhage. *Stroke* **1998**, *29*, 2580–2586.

[70] Xi, G. H.; Reiser, G.; Keep, R. F. The role of thrombin and thrombin receptors in ischemic, hemorrhagic and traumatic brain injury: Deleterious or protective? *J. Neurochem.* **2003**, *84*, 3–9.

[71] Wu, H.; Wu, T.; Xu, X. Y.; Wang, J.; Wang, J. Iron toxicity in mice with collagenase-induced intracerebral hemorrhage. *J. Cereb. Blood Flow Metab.* **2011**, *31*, 1243–1250.

[72] Sykora, M.; Diedler, J.; Turcani, P.; Rupp, A.; Steiner, T. Subacute perihematomal edema in intracerebral hemorrhage is associated with impaired blood pressure regulation. *J. Neurol. Sci.* **2009**, *284*, 108–112.